Super-Resolution in Respiratory Synchronized Positron Emission Tomography

Daphné Wallach , Frédéric Lamare, Giorgos Kontaxakis, and Dimitris Visvikis,

Abstract—Respiratory motion is a major source of reduced quality in positron emission tomography (PET). In order to minimize its effects, the use of respiratory synchronized acquisitions, leading to gated frames, has been suggested. Such frames, however, are of low signal-to-noise ratio (SNR) as they contain reduced statistics. Super-resolution (SR) techniques make use of the motion in a sequence of images in order to improve their quality. They aim at enhancing a low-resolution image belonging to a sequence of images representing different views of the same scene. In this work, a maximum a posteriori (MAP) super-resolution algorithm has been implemented and applied to respiratory gated PET images for motion compensation. An edge preserving Huber regularization term was used to ensure convergence. Motion fields were recovered using a B-spline based elastic registration algorithm. The performance of the SR algorithm was evaluated through the use of both simulated and clinical datasets by assessing image SNR, as well as the contrast, position and extent of the different lesions. Results were compared to summing the registered synchronized frames on both simulated and clinical datasets. The super-resolution image had higher SNR (by a factor of over 4 on average) and lesion contrast (by a factor of 2) than the single respiratory synchronized frame using the same reconstruction matrix size. In comparison to the motion corrected or the motion free images a similar SNR was obtained, while improvements of up to 20% in the recovered lesion size and contrast were measured. Finally, the recovered lesion locations on the SR images were systematically closer to the true simulated lesion positions. These observations concerning the SNR, lesion contrast and size were confirmed on two clinical datasets included in the study. In conclusion, the use of SR techniques applied to respiratory motion synchronized images lead to motion compensation combined with improved image SNR and contrast, without any increase in the overall acquisition times.

Index Terms—Four-dimensional (4-D) positron emission tomography, respiratory motion, super-resolution.

I. INTRODUCTION

P OSITRON emission tomography (PET) is widely used today for diagnosis and therapy follow up assessment in oncology. This functional imaging technique often allows detection of lesions that are not visible on anatomical imaging

*D. Wallach is with the INSERM, U650, LaTIM, CHU Morvan, Brest F-29200, France (e-mail: daphne.wallach@etudiant.univ-brest.fr).

F. Lamare is with the CHU de Bordeaux, Pole d'imagerie, Bordeaux F-33076, France, and also with the Université de Bordeaux, INCIA, CNRS UMR 5287, Bordeaux, France (e-mail: frederic.lamare@chu-bordeaux.fr).

G. Kontaxakis is with the ETSI Telecomunicaciòn, Universidad Politécnica de Madrid, 28040 Madrid, Spain, and also with the Networking Research Centrer on Bioengineering, Biomaterials and Nanomedicine (CIBER-BBN), Madrid, Spain (e-mail: gkont@die.upm.es).

D. Visvikis is with the INSERM, U650, LaTIM, CHU Morvan, Brest F-29200, France (e-mail: dimitris@univ-brest.fr).

such as computed tomography (CT) or magnetic resonance imaging (MRI). Although diagnosis is mainly based on visual assessment of abnormal activity concentrations, quantitative analysis facilitates comparisons between patients and is necessary in therapy response assessment studies. Respiratory motion is one of the issues that hinder such analysis, particularly when one considers thoracic imaging. Respiratory motion has been shown to reduce accuracy in determining both functional lesion volumes and associated recovered activity concentrations [1]. Furthermore, the use of multi-modality imaging devices combining anatomical and functional imaging has revealed various artifacts in the functional images caused by the mismatching in terms of respiratory motion state between the emission tomography datasets and the anatomical images used for their attenuation correction [2], [3].

In order to minimize the effects of motion due to respiration, the use of respiratory synchronized acquisitions has been proposed, leading to a number of gated frames corresponding to different parts of the respiratory cycle [4]. Different devices have been used to provide the 1-D patient respiratory signal necessary for the synchronization process, with binning of the acquired datasets carried out using either the motion phase or amplitude. In general, the resulting respiratory synchronized PET images are of low signal-to-noise ratio (SNR), as for a time equivalent acquisition they contain reduced statistics with respect to a respiratory motion average acquisition. Therefore motion compensation approaches have been developed allowing the combination of these synchronized datasets to a particular part of the respiratory cycle, hence making use of all the available statistics. Most existing compensation techniques follow a register-and-sum approach, with transformation maps derived either from 4-D CT or gated PET datasets [5]–[7]. Assuming an affine motion model, these transformations have been applied to correct the raw data prior to reconstruction [7], [8]. On the other hand, elastic motion models can be incorporated into the reconstruction process to directly reconstruct a motion-corrected image from the gated data [9], [10].

An alternative to correcting for the effects of respiratory motion is to use the motion information derived from respiratory synchronized datasets to improve the overall PET image quality. One methodology that can be employed within this context is super-resolution. Super-resolution techniques aim at producing a high-resolution (HR) image from a set of low-resolution (LR) images, each providing slightly different spatial information [11]. Their primary aim is to use motion information to enhance the quality of the image sequence by taking advantage of the additional spatio-temporal information. By registering all LR images to a common position and superimposing them, sub-pixel information can be recovered,
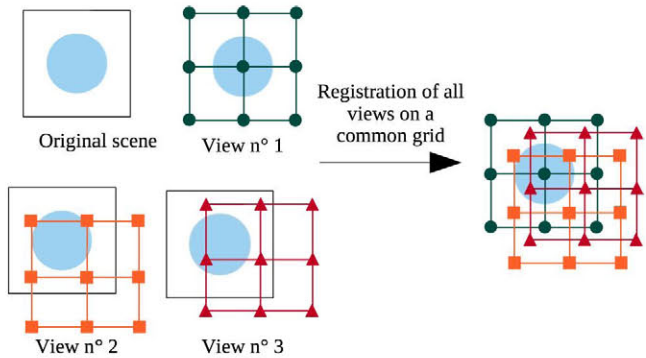
Fig. 1. Graphical representation of the sub-pixel information than can be obtained during the super-resolution process through the combination of different matrices associated with different views of the same object.

as is illustrated in Fig. 1. This additional information enables reconstruction of a super-resolved image with wider bandwidth than that of any of the individual LR frames.

Different methods have been proposed over the years to compensate for the under-sampling problem of PET acquisitions. One of them consisted of physically moving the scanner (known as "wobbling") leading to finely sampled projections [12]. Wernick and Chen [13] showed that further resolution enhancement could be obtained by applying a super-resolution approach to the individual LR sinograms acquired by the scanner "wobbling" technique. A filtered back-projection reconstruction algorithm was then applied to the SR enhanced sinogram, yielding a substantially improved image in terms of contrast and SNR. Later, Kennedy *et al.* [14] created multiple LR frames by shifting and rotating an object during the acquisition and showed an increase in both resolution and contrast. Similar results were seen in a clinical PET study by moving the bed by sequential 1 mm steps in the axial direction [15]. In order to reduce the increase in acquisition time and complexity of implementation, Chang *et al.* [16] proposed a method enabling the creation of different frames from a standard acquisition. This was achieved by shifting the reconstruction grid, hence creating an image sequence from a single acquisition, demonstrating contrast and resolution improvements similar to those obtained by moving the object during imaging [17]. However, shifting the reconstruction grid was also found to yield lower SNR than moving the object, since only one noise realization was acquired [17].

All these implementations explored an "artificially" created image sequence (scanner, bed, or reconstruction matrix displacement) in order to perform super-resolution in PET imaging. On the other hand, the presence of physiological motion such as for example respiratory motion forms naturally part of the acquired PET datasets. Therefore, in principle PET respiratory synchronized datasets can be used to improve overall PET image quality through the super-resolution approach. Another advantage of using the respiratory gated frames to perform super-resolution, relative to the previously implemented approaches, is that several frames with independent noise contents can be obtained using a standard 4-D PET acquisition protocol.

The objective of the present study was to evaluate the application of a maximum a posteriori (MAP) super-resolution algorithm to the respiratory gated PET images in order to derive a high resolution 4-D PET image sequence. The performance of the algorithm was evaluated through the use of both simulated and clinical datasets by assessing image SNR as well as lesion contrast, position and spatial extent.

II. MATERIALS AND METHODS

The use of super-resolution techniques in PET imaging has been restricted to date to the use of the iterative back-projection (IBP) [18] and the projection onto convex sets (POCS) super-resolution algorithms [19]. At each iteration of the IBP algorithm, the current estimate of the super-resolved image is registered to the LR images, down-sampled and compared to the corresponding LR image. The difference between the LR images and the degraded super-resolved image is used to update the super-resolved image through a back-projection operator. Although conceptually simple, IBP suffers from a number of disadvantages [20]. More specifically, the result is highly dependent on the backprojection operator, while neither the existence nor the uniqueness of the solution is guaranteed. Furthermore, with IBP it is impossible to introduce regularization in the super-resolution process. The POCS algorithm considers each constraint as a convex set in the space of all possible solutions. At each iteration of the POCS algorithm, the current estimate of the HR image is projected onto one of these convex sets. Like IBP, the result of this algorithm is highly dependent on the choice of convex sets, while neither the existence nor the uniqueness of the solution is guaranteed. Furthermore, it has a high computational cost. On the other hand, MAP as a stochastic method incorporates *a priori* knowledge about the problem's solution acting as regularization in order to make it well-posed [21]–[23]. Regularization in MAP can model a large variety of desired properties of the solution, such as local or global smoothness, finite energy, sharp edges, etc. The convergence of the algorithm makes the final result independent of the initial image. Moreover, in the implementation of the MAP super-resolution algorithm a model of the blurring associated with the finite resolution of the PET detectors can be incorporated, which is expected to yield further resolution enhancement. For all these reasons the MAP algorithm was selected for the implementation of the super-resolution technique in this work.

A. MAP Super-Resolution

The MAP super-resolution algorithm consists in inverting an observation model relating the LR images to the HR image (see Fig. 2). Consider the 3-D HR image of size $L_1 N_1 \times L_2 N_2 \times L_3 N_3$, written as the vector f. It is the ideal image that results from sampling (at or above the Nyquist rate) a continuous, band-limited 3-D scene. The parameters L_1, L_2, and L_3 represent the down-sampling factors in the observation model for each of the three directions. Thus, each of the K observed LR images is of size $N_1 \times N_2 \times N_3$ and is denoted in lexicographical notation as $y_k, k = 1$ to K. The observed LR images result from warping, blurring and subsampling of the HR image f, including an additive noise term (see Fig. 2). The dimensions
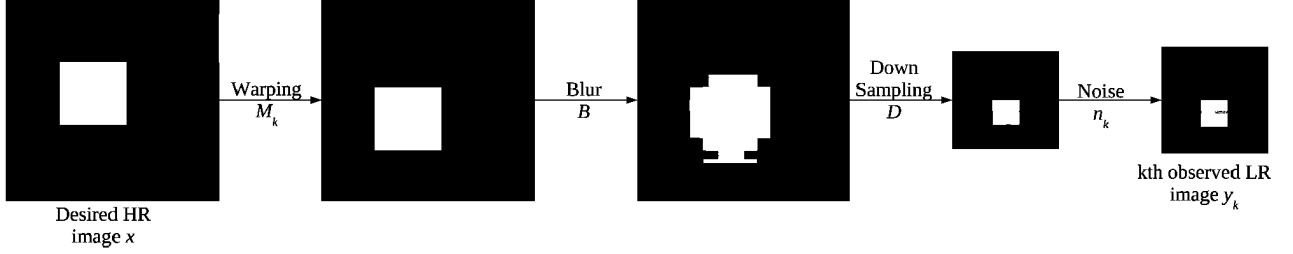
Fig. 2. Observation model used in the super-resolution algorithm implementation.

of HR and LR images will be denoted from here onwards by $N_{\mathrm{HR}} = L_1 N_1 \times L_2 N_2 \times L_3 N_3$ and $N_{\mathrm{LR}} = N_1 \times N_2 \times N_3$. The vector f is of size N_{HR}, while vectors y_k are of size N_{LR}.

The observation model can be written as

$$y_k = DBM_k f + \varepsilon_k, k = 1 \cdots K \tag{1}$$

where D is a $N_{\mathrm{LR}} \times N_{\mathrm{HR}}$ subsampling matrix performing an averaging over neighboring voxels, B is a $N_{\mathrm{HR}} \times N_{HR}$ space invariant blur matrix that models the action of the point spread function of the PET system, M_k is a $N_{\mathrm{HR}} \times N_{HR}$ warp matrix containing the motion between frame 1 and frame k, and ε_k is a noise vector. The operators D, B, and M_k are known (computation of M_k is detailed in Section II-B), and the LR images y_k correspond in our application to the respiratory synchronized PET image series. The aim of super-resolution is the recovery of the HR image f. This is done by maximizing its a posteriori probability, that is to say the probability of f given the y_k. The estimator of the HR image, f, is given by

$$f = \arg\max_f p\left(f | y_1, y_2, \ldots, y_K\right) \tag{2}$$

$$= \arg\max_f \prod_{k=1}^{K} p\left(f | y_k\right). \tag{3}$$

According to Bayes formula, $p(f|y_k) = p(y_k|f)p(f)/p(y_k)$. Since f does not depend on $p(y_k)$, this yields

$$f = \arg\max_f \prod_{k=1}^{K} p(y_k|f)p(f) \tag{4}$$

$$= \arg\min_f \sum_{k=1}^{K} -\ln p(y_k|f) - \ln p(f). \tag{5}$$

Considering the noise ε_k comes from multiple independent sources, the central limit theorem states that its distribution converges to a Gaussian distribution as the number of sources increases. In this work, assuming that there are enough independent sources of noise to consider we assume that their sum follows a Gaussian distribution with a zero mean. In this case, the conditional density $p(y_k|f)$ is given by

$$p(y_k|f) = \frac{1}{\sqrt{2\pi\sigma_k^2}^{N_{\mathrm{LR}}}} \exp\left(-\frac{1}{2\sigma_k^2}\|y_k - DBM_k f\|^2\right) \tag{6}$$

where σ_k is the standard deviation of the noise in the kth LR image.

The *a priori* image model $p(f)$ represents *a priori* knowledge about the HR image. It is often chosen as a Gibbs distribution over a Markov random field. Its probability density is defined as

$$p(f) = \frac{1}{Z} \exp\left(-\sum_{c \in \mathcal{S}} V_c(f)\right) \tag{7}$$

where Z is a normalizing constant, $\mathcal{S}$ denotes the set of cliques, and V_c is an energy function depending only on the pixel values located within clique c. Here, we chose a six-neighborhood system. Assuming the HR image is globally smooth with sharp edges, we choose a Huber energy function

$$V_\delta(z) = \begin{cases} z^2, & \text{if } |z| < \delta \\ 2\delta|z| - \delta^2, & \text{if } |z| \geq \delta \end{cases} \tag{8}$$

where δ is a positive parameter controlling the switch between the quadratic and the linear part of the function. This function is quadratic near the origin and linear far from the origin, which means that small intensity differences between neighboring voxels are more penalized than large ones, which we assume are due to signal rather than noise.

Finally, the function to minimize is

$$F(x) = \sum_{k=1}^{K} \|y_k - DBM_k f\|^2 + \lambda \sum_{i=1}^{N_{HR}} \sum_{j \in \mathcal{N}_i} V_\delta(f_i - f_j) \tag{9}$$

where λ is a positive parameter controlling the balance between the data-fidelity term and the regularizing term and $\mathcal{N}_i$ is the neighborhood of the voxel i. F is minimized using a quasi-Newton algorithm.

B. Motion Fields

The warp matrices are obtained through the application of an elastic registration algorithm to the gated PET frames [24]. Let us denote the individual frames as functions of sets of coordinates, $y_k(x)$. For a particular set of coordinates $x \in \mathbf{R}^3$, $y_k(x)$ is the intensity of the kth image at position x. The elastic registration is defined as a function g_k of sets of coordinates x such that

$$y_k(x) = y_1\left(g_k(x)\right). \tag{10}$$

It maps a position in frame k onto a position in frame 1. The function g_k is chosen as a spline. Splines are smooth piecewise polynomials that can be uniquely expressed as a weighted sum of a shifted B-spline. Due to their small number of parameters as well as regularity and ability to represent deformable motion,

splines are often used to model respiratory motion [9], [10]. The function g_k can thus be expressed as a linear combination of B-spline basis functions located on a rectangular grid

$$g_k(x) = x + \sum_{j \in \mathbf{Z}^3} c_j \beta \left(\frac{x}{h} - j \right) \qquad (11)$$

where β is a tensor product of centered cubic B-splines, $j \in \mathbf{Z}^3$ are the indices of the grid locations, $h \in \mathbf{R}$ is the spacing between two grid nodes, and the weights $c_j \in \mathbf{R}$ are the parameters to be optimized.

The deformations g_k are calculated for every k on the PET respiratory synchronized images. They are calculated at every point x in order to create the warp matrices M_k, and applied to the HR image (see (1), matrix M_k). Although the registration is performed on the low-resolution images, applying its result to the high resolution image requires no additional interpolation, since the functions g_k are continuous with respect to x.

C. Evaluation Datasets

Five simulated and two clinical datasets were used in order to evaluate the performance of the proposed method and assess the influence of the regularization parameters. The simulated datasets were produced using a digital model of the Philips GEMINI PET system implemented in GATE [25].

The first simulated dataset consisted of six frames of the IEC phantom [26], each shifted by 3 mm along the z-axis relative to each other. The IEC phantom is a water filled cylinder of radius 10 cm containing six coplanar spheres of radii 10, 13, 17, 22, 28, and 37 mm. A sphere to background ratio of 4 to 1 was used. Fifteen second acquisitions were simulated for each noise realization of each frame.

The other simulated datasets were produced using the digital NURBS-based 4-D cardiac-torso phantom (NCAT, [27]). The two first simulated datasets used the default anatomy and respiratory cycle of NCAT. For each simulation, a set of eight emission images was produced throughout a sinusoidal respiratory cycle (0.625 s per frame considering a normal respiratory cycle of 5 s). The maximum motion amplitude of the diaphragm was set to 20 mm in the craniocaudal direction. Spherical lesions of different sizes were added to the NCAT emission and attenuation images [7]. These lesions were 7 and 11 mm across for the first simulated sequence and 15 and 21 mm for the second. Normal FDG activity levels were placed in the lung and liver, while a tumor to background ratio of 8 to 1 was used. A total number of 5.4 million detected coincidences were simulated for each of the eight temporal frames. The simulated count statistics correspond to the statistics of a standard clinical acquisition (3 min per axial field-of-view) using the PET system simulated in this study. In addition, motionless datasets corresponding to the first NCAT emission frame were obtained for each of the two phantoms by simulating a total of 43.2 million coincidences (i.e., equivalent to the total coincidences simulated throughout a respiratory average acquisition of eight frames with 5.4 million detected coincidences in each frame). The list-mode data output of the simulation was used. All images were reconstructed using the OPL-EM algorithm [28] with a voxel size of $1.56 \times 1.56 \times 1.56$ mm^3 and $3.12 \times 3.12 \times 3.12$ mm^3 for the first and second

dataset respectively. Attenuation correction was included in the reconstruction process using for each frame the corresponding attenuation map used in the simulation process.

The two other simulated datasets were obtained by incorporating patient specific modifications to the NCAT phantom as previously described by Le Maitre *et al.* [29], using patient specific anatomy and respiratory motion. The simulated maximum diaphragm displacement was 15 and 25 mm for the two simulated datasets. A realistic lesion segmented manually from patient FDG images was finally added to each of the two pair of emission and attenuation datasets. The first was a circular lesion with a necrotic core (tumor/background contrast of 20/1, outer diameter of 40 mm and necrotic center with a maximum length of 20 mm). The second dataset had a heterogeneous, crescent-shaped tumor with a contrast of 2.5 and 9 between the high and low uptake regions and between the low uptake region and the background activity, respectively. The high uptake region of the lesion was approximately circular, with an 18 mm diameter. Approximately 46.5 million detected coincidences were simulated for the first dataset, and 41.6 million for the second one, corresponding to three minute acquisitions per axial field of view for both datasets. Eight synchronized PET images were reconstructed using 4 mm voxels (in all three dimensions). Motionless datasets were also obtained by simulating 3 min acquisitions of the first respiratory frame for each of these two phantoms. Attenuation correction was performed using the attenuation images used in the simulations process.

The two clinical datasets used in this study were lung cancer patients undergoing FDG whole body acquisitions on a GE Discovery ST PET/CT scanner operating in 3-D mode using 3 min of acquisition per bed position. Respiratory motion was monitored using a real-time position management device (RPM, Varian Medical Systems) and the data were binned in ten phase based respiratory frames. A 4-D CT acquisition was used to correct each PET frame for attenuation. Finally, the PET images were reconstructed using OSEM with $5.45 \times 5.45 \times 3.26$ mm^3 voxels. The maximum diaphragm displacement amplitude in the craniocaudal direction measured on the 4-D CT image series for the two patients considered was approximately 6.3 ± 3.2 mm.

D. Data Analysis

In order to evaluate the influence of the regularization parameters λ and δ, the proposed super-resolution method was applied to the six frames of the IEC phantom with variable regularization parameters ($\lambda = 0.01, 0.1, 1, 10, 100$, and $\delta = 0.01, 0.1, 1, 10$). Convergence speed was measured through the number of iterations required before the step between two successive points was $< 10^{-8}$.

For each of the anthropomorphic simulated datasets, seven images were compared.
  (a) *Frame 1* image corresponding to the first frame of the gated sequence,
  (b) *Large Frame 1* image, corresponding to the same frame as (a). above reconstructed using the same matrix size as the super-resolution image (i.e., twice as large as the original frame in every direction),
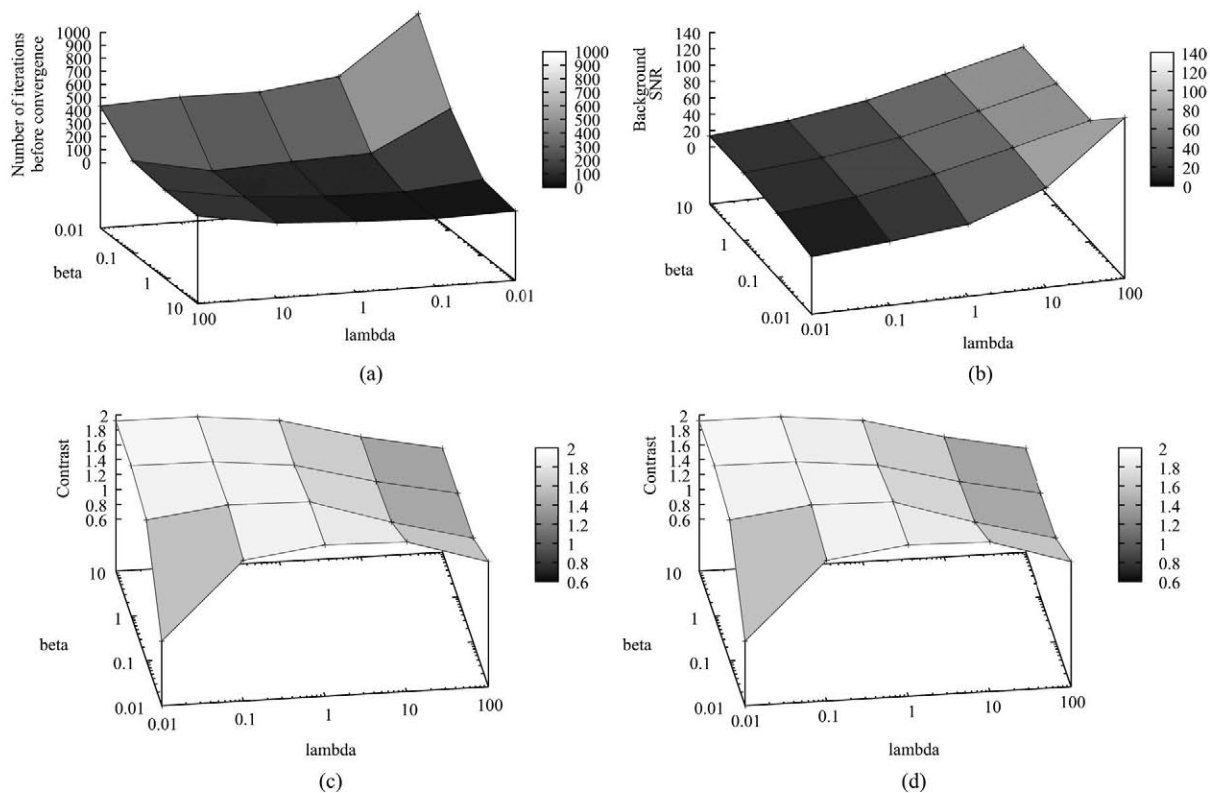
Fig. 3. (a) Number of iterations to convergence. (b) Background SNR. (c) Contrast and (d) FWHM for the 22 mm lesion with respect to the regularization parameters.

(c) *All Counts* image, corresponding to the same respiratory position as frame 1 (image (a). above) but reconstructed using the entire respiratory cycle count statistics,

(d) *Motion Average* image reconstructed using the list mode files corresponding to all the gated frames (counts are summed in the raw data space before reconstruction),

(e) *Sum of Registered Frames* image, corresponding to the sum of all reconstructed gated frames registered to frame 1,

(f) *SR* image, corresponding to the output of the proposed algorithm,

(g) *SR without PSF modeling* image, obtained with a version of the proposed algorithm where the blur term was not considered, i.e., matrix B is removed from (1).

In the case of the clinical datasets the comparison was performed considering only the images corresponding to (a), (d), (e), (f), and (g). The image corresponding to case (b) could not be reconstructed for the clinical datasets because the raw data was not available, while the long acquisition times necessary to reproduce the respiratory synchronized image (c) of the simulated datasets was not compatible with clinical routine acquisitions.

For all of the datasets considered image quality was assessed through evaluation of the lesions' contrast and signal-to-noise ratio. Resolution was assessed through the measurement of the full-width at half-maximum (FWHM) for each lesion. Finally, for the simulated images, the position error of each lesion was also calculated. In order to measure contrast and SNR, regions of interest (ROIs) were drawn over each of the lesions and in the background lung. The slice with the maximum count density over the lesion was identified and the lesion ROI was placed in this slice. In order to limit partial volume effects, the ROI sizes used were set to 70% of the true lesion size and of the maximum count density in the simulated and clinical datasets respectively. In the case of the lung four 2 cm ROIs were placed throughout the lung fields. SNR was computed as the ratio of the mean over the standard deviation of intensities for the different ROIs in the lungs. Contrast was calculated as the ratio of the mean intensity in the lesion ROI to the mean intensity of the lung ROIs. For the assessment of lesion position and FWHM, a rectangular box was placed along the diameter of each tumor in the craniocaudal direction. A Gaussian function was then used to approximate the tumor line profile defined as the mean profile along this box. Position and FWHM of the lesions were derived from the center and the standard deviation of the Gaussian fit.

III. RESULTS

The influence of the regularization parameters on convergence and image quality was assessed using the results presented in Fig. 3. Since contrast and FWHM results were similar for all spheres, only the ones concerning the 22 mm sphere were presented in this figure. All problems with a nonzero value of λ were found to converge to a unique solution. Globally, background SNR, contrast and FWHM were more sensitive on λ than on δ. As expected, background SNR was higher for higher values of λ (+64.5% to +90.6% when λ is multiplied by 10). However, as δ increases, background SNR stays within 5% of the same value. Conversely to background SNR, lesion contrast increases with λ between 0.01 and 0.1 (an average increase of 17.9%), while lesion contrast decreases
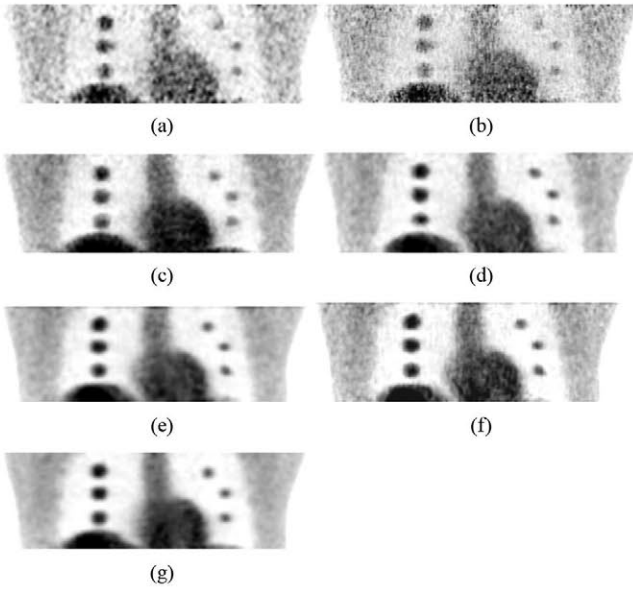
(a)

(b)

(c)

(d)

(e)

(f)

(g)

Fig. 4. Comparison of different NCAT reconstructed images (incorporating the 15 and 21 mm lung lesions), corresponding to (a) single respiratory synchronized frame (*Frame 1*), (b) same as (a) using a matrix size twice as large in every direction (*Large Frame 1*), (c) motion average frame (*Motion Average*), (d) sum of registered synchronized frames (*Sum of Registered Frames*), (e) super-resolution (*SR*) image, (f) SR image obtained without PSF modeling, and (g) same position as (a) reconstructed using the entire respiratory cycle count statistics (*All Counts*).

for $\lambda > 0.1$ (-1.4% to -16.0%). Once again, variations of δ lead only to moderate variations of contrast (-1% to 5.9%). Concerning FWHM, increases in both λ and δ lead to increased estimated lesion size, although variations with respect to λ are of larger amplitude than variations with respect to δ (34.6% ± 27.4% versus 23.3% ± 25.9%).

The super-resolution images were computed with an upsampling set to 2 in every direction. The regularization parameters λ and δ for each of the simulated anthropomorphic and clinical datasets were chosen in order to achieve both high SNR and high contrast. Convergence was not a criterion since all problems with a nonzero λ were found to converge to a unique solution. For all simulated and clinical datasets $\lambda = 0.6$ and $\delta = 1$ were used. The second simulated dataset, being reconstructed with smaller voxels and similar statistics as the other simulated datasets resulted in noisier frames and hence required more regularization ($\lambda = 1.2$ and $\delta = 2$).

Fig. 4 presents a comparison of the seven different reconstructed images of the simulated NCAT phantom with the spherical lung lesions considered in the evaluation (see Section II-D). For these same NCAT simulated datasets, Table I contains the results of the quantitative analysis on the SNR, contrast, and FWHM as a function of lesion size.

The use of only part of the statistics associated with the synchronized images (*Frame 1*) leads to a lower SNR by a factor of 1.5–3 and 1.1–2 relative to the image corresponding to the same frame reconstructed with the entire respiratory cycle count statistics (*All Counts* image) and the *Motion Average* image respectively. A higher resolution synchronized frame image (*Large Frame 1*) leads to the worst SNR with a reduction by ~ 70% relative to the standard reconstruction matrix (*Frame 1*). Finally the

super-resolution frames, computed with or without PSF modeling (*SR* and *SR without PSF modeling*) lead to an SNR equivalent to that of the images derived either from the sum of the images realigned to the same frame in the respiratory cycle (*Sum of Registered Frames*) or from the same frame reconstructed with the entire respiratory cycle count statistics (*All Counts* image).

In terms of lesion contrast, the reduced SNR associated with the *Large Frame 1* leads to the worst lesion contrast performance, with a reduction of 15%–30% (depending on the lesion size) relative to the standard synchronized image *Frame 1*. On the other hand, the *Frame 1* image exhibits similar contrast compared to the *Motion Average* image (~ 10% differences throughout the range of lesion sizes considered), demonstrating that the gain of reducing respiratory motion effects is practically cancelled by the reduced statistics associated with a single synchronized frame image. The lesion contrast performance of the *Sum of Registered Frames* image was very close (< 3%) to that of the *All Counts* images. Finally, the highest contrast was associated with the SR images, particularly when the modeling of the scanner PSF was included. Lesion contrast in the *SR* and *SR without PSF modeling* images was respectively up to 15% and 10% higher than in the *All Counts* image.

The motion average reconstructed image systematically yielded the largest recovered lesion size, with a FWHM larger than that of the *All Counts* images by on average 44%, 26%, 37%, and 31% for the 7, 11, 15, and 21 mm lesions, respectively. In addition, this same image was associated, as a result of the respiratory motion effects, with the largest variability in the recovered lesion size as a function of their placement in the different parts of the lung field. On the other hand, differences in the recovered lesion sizes were on average between 7% and 12% between the respiratory synchronized image (*Frame 1*) and the *All Counts* image, increasing to 14%–24% for the high resolution respiratory synchronized image (*Large Frame 1*). More importantly, this image showed an increase by over a factor of 2 in the variability of the recovered size throughout the lung fields when compared to the standard *Frame 1*. This increased variability was most probably caused by uncertainties associated with the measured decrease in the SNR highlighted above in this same section.

Considering the respiratory motion corrected images, the recovered lesion sizes from the *Sum of Registered Frames* image were within 5% of the ones obtained using the *All Counts* image for the entire range of lesion sizes considered. The associated variability was similar to that obtained for the *Frame 1* or the *All Counts* images. Finally, the smallest FWHM and associated variability as a function of lesion location was measured with the SR images, particularly noticeable for the smaller size lesions (7–11 mm), with average differences of up to -18% relative to the *All Counts* image. The advantage of PSF modeling within the super-resolution process was mostly seen for the smaller lesion sizes, with an 8% larger FWHM measured in the *SR without PSF modeling* image. On the other hand, the FWHM of the larger lesions was similar (differences < 2%) in both images.

Figs. 5 and 6 show a comparison of the lesion images in the different reconstructions considered for the patient specific NCAT phantom simulations (see Section II-C). A quantitative analysis in terms of SNR, contrast, FWHM, and position error

SNR	7 mm lesions	11 mm lesions	15 mm lesions	21 mm lesions	All lesions	Background
Frame 1	7.27±0.96	4.19±0.72	5.04±0.60	4.17±0.34	5.17±1.44	3.72±0.37
Large Frame 1	2.65±0.27	1.86±0.08	3.95±0.69	4.59±0.37	3.26±1.17	2.86±1.48
Motion AveragE	10.13±3.63	8.42±0.20	5.29±0.39	6.36±1.83	7.55±2.62	8.27±0.82
Sum of Registered Frames	18.01±6.09	11.16±0.80	6.70±1.64	6.81±1.24	10.67±5.55	10.43±0.45
SR	20.70±7.26	11.15±1.06	8.20±1.39	7.54±1.37	11.90±6.38	10.74±0.21
SR without PSF modeling	20.36±6.28	11.07±0.77	7.26±0.85	6.92±0.60	11.40±6.29	10.71±1.21
all Counts	20.61±5.54	10.76±0.71	7.79±0.80	7.44±1.65	11.65±6.11	10.50±2.08
Contrast						
Frame 1	0.85±0.05	0.97±0.17	2.36±0.09	3.35±0.22	1.88±1.09	
Large Frame 1	0.73±0.06	0.72±0.01	1.92±0.14	2.43±0.24	1.45±0.79	
Motion Average	0.95±0.05	1.08±0.04	2.14±0.10	3.23±0.34	1.85±0.91	
Sum of Registered Frames	1.17±0.06	1.24±0.02	2.47±0.12	3.54±0.19	2.11±1.02	
SR	1.37±0.09	1.36±0.07	2.85±0.12	3.86±0.32	2.36±0.97	
SR without PSF modeling	1.28±0.10	1.31±0.11	2.73±0.03	3.72±0.29	2.26±1.08	
All Counts	1.21±0.09	1.25±0.05	2.48±0.23	3.44±0.18	2.10±0.99	
FWHM (mm)						
Frame 1	13.11±1.92	15.77±0.98	16.53±2.80	22.82±1.45	17.06±2.96	
Large Frame 1	13.85±2.46	16.97±3.45	18.82±7.31	24.28±2.12	18.48±5.16	
Motion Average	16.86±3.71	18.68±1.85	20.77±0.26	27.80±1.05	21.03±3.36	
Sum of Registered Frames	12.32±3.45	14.23±1.98	15.13±0.69	20.44±1.23	15.53±2.94	
SR	9.76±2.46	13.04±0.98	14.89±0.31	20.52±0.73	14.55±1.79	
SR without PSF modeling	10.55±1.48	13.46±0.19	14.99±0.46	20.90±0.38	14.87±2.08	
All Counts	11.71±2.24	14.67±1.63	15.50±0.31	21.25±0.61	15.76±2.51	

is presented in Tables II and III for the two lesion images shown in Figs. 5 and 6, respectively. The results are largely in agreement with what was observed for the first two simpler NCAT simulated sequences. Once again, *Frame 1* and *Large Frame 1* images exhibit lower SNR since they contain less statistics than the other images, with the *Large Frame 1* image leading to the worst SNR (-20% to -50% relative to *Frame 1*) as a result of the noise amplification associated with the use of the smaller reconstructed pixel size. One the other hand, the *Motion Average* image showed a level of SNR similar to that of the *All Counts* image, while the best SNR was associated with the respiratory motion corrected images (*Sum of Registered Frames, SR, and SR without PSF modeling*). In terms of image contrast smaller differences were seen in performance between the different reconstructed images for each of the two simulated datasets. The worst contrast (between -10% and -20% relative to the *All Counts* image) was the one obtained from the *Motion Average* and the *Large Frame 1* images. Globally similar levels of contrast ($< 8\%$) were seen in the images accounting for the effects of the respiratory motion (*Sum of Registered Frames, SR and SR without PSF modeling*). Concerning the lesion size and location the SR images allowed the best accuracy, being closer to the real simulated lesion sizes (26 mm and 18 mm for the tumor slice location considered on the first and second simulated dataset, see Figs. 5 and 6) and localizations as well as to the results obtained using the *All Counts* image. Although globally a similar performance was obtained using the *Sum of Registered Frames* images, there was a larger variability with lesion location in the accuracy of the results concerning both the recovered lesion size and position. Finally, although the use of

respiratory gating led to better results than the *Motion Average* image, the increased noise levels associated with the lower statistical quality for *Frame 1* and *Large Frame 1* images compromised the accuracy of determining both the lesion size and associated location, explaining the higher FWHM and position errors observed.

The images obtained for the two clinical datasets are presented in Figs. 7 and 8. Corresponding quantitative results of SNR, contrast, and FWHM assessing lesion size are presented in Table IV. As a result of the reduced statistics the respiratory synchronized images led to the worst SNR (-10% to -30%) relative to the respiratory average or respiratory motion corrected (*Sum of Registered Frames, SR* and *SR without PSF modeling*) images. The SR images led systematically to the highest SNR compared to the *Motion Average* ($11.2\% \pm 9.2\%$) and *Sum of Registered Frames* ($5.0\% \pm 3.6\%$) images. In terms of both contrast and FWHM there were only small differences between the respiratory synchronized *Frame 1* and the *Motion Average* image. The highest lesion contrast was obtained using the SR image with PSF modeling compared to the *Motion Average* ($60.2\% \pm 24.1\%$) and *Sum of Registered Frames* ($34.2\% \pm 19.6\%$) images. Similar trend but with smaller magnitude differences ($11.4\% \pm 6.8\%$ and $8.6\% \pm 9\%$ compared to the *Motion Average* and the *Sum of Registered Frames* images, respectively) were obtained for the lesion size measurements.

IV. DISCUSSION

Respiratory motion in PET/CT imaging is responsible for a reduction in overall image quality associated with a loss of both quantitative and qualitative accuracy. Proposed solutions are
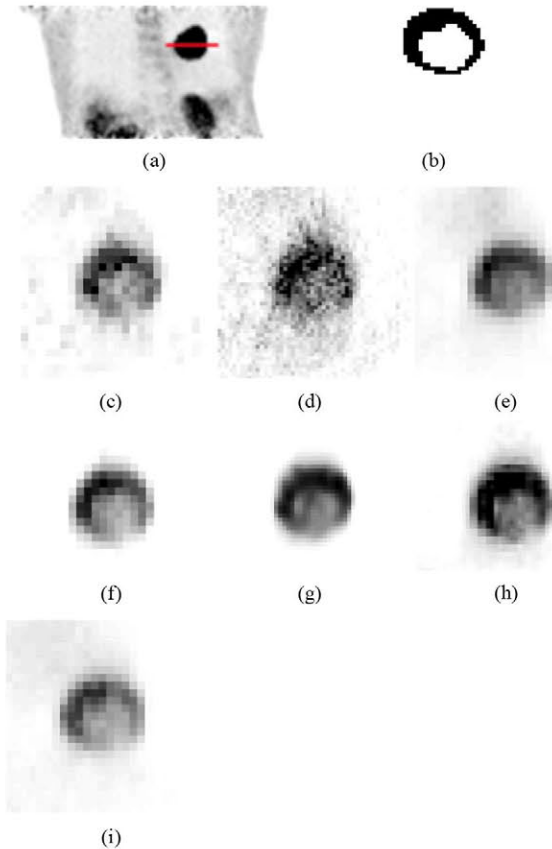
Fig. 5. Data from the first patient specific NCAT simulated dataset, showing (a) a coronal view of a single PET gated frame image, and (b) a transverse view of the simulated tumor along the profile shown in (a) Comparison of the different reconstructed tumor images, considering the (c) single gated frame (*Frame 1*), (d) same as (c) using a matrix size twice as large in every direction (*Large Frame 1*), (e) motion average frame (*Motion Average*), (f) sum of registered synchronized frames (*Sum of Registered Frames*), (g) super-resolution (*SR*) image, (h) SR image obtained without PSF modeling, and (i) same position as (c) reconstructed using the entire respiratory cycle count statistics (*All Counts*).
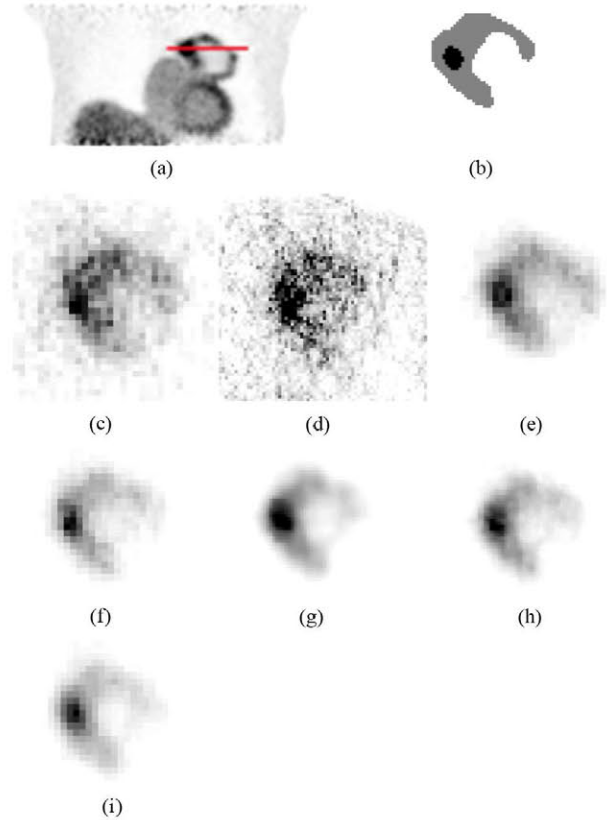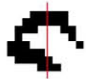

Fig. 6. Data from the second patient specific NCAT simulated dataset, showing (a) a coronal view of a single PET gated frame image, and (b) a transverse view of the simulated tumor along the profile shown in (a). Comparison of the different reconstructed tumor images, considering the (c) single gated frame (*Frame 1*), (d) same as (c) using a matrix size twice as large in every direction (*Large Frame 1*), (e) motion average frame (*Motion Average*), (f) sum of registered synchronized frames (*Sum of Registered Frames*), (g) super-resolution (*SR*) image, (h) SR image obtained without PSF modeling, and (i) same position as (c) reconstructed using the entire respiratory cycle count statistics (*All Counts*).

based on the use of respiratory synchronized acquisitions which reduce the effects of respiratory motion. However, such gated acquisitions are also associated with an increase in PET image statistical noise since only part of the data available throughout a respiratory motion average acquisition is used. In order to account for these effects the synchronized gated datasets can be combined using deformable image registration applied either during or after the reconstruction of the respiratory synchronized datasets.

An alternative approach is proposed in this work based on the use of a MAP super-resolution algorithm. The principle of super-resolution is to use motion information derived from an image sequence representing different views of the same scene to enhance the quality of the image sequence by taking advantage of the additional spatio-temporal information available. In the proposed methodology motion information inherent in the respiratory synchronized PET image frames is combined with a MAP super-resolution algorithm. The proposed algorithm was assessed using both simple and patient specific anthropomorphic simulated datasets and was tested on a couple of clinical PET studies.

TABLE II
BACKGROUND SNR, AND LESION CONTRAST, FWHM AND POSITION ERROR (BOTH MEASURED IN MM) USING THE RECONSTRUCTED IMAGES OF THE FIRST PATIENT SPECIFIC NCAT SIMULATED DATASET. VALUES OF FWHM AND POSITION ERROR WERE MEASURED IN THE CRANIOCAUDAL DIRECTION, ALONG THE PROFILE SHOWN ON THE SIMULATED LESION BINARY IMAGE SHOWN ON THE TABLE

	SNR B	Contrast T/B	FWHM (mm)	Position error (mm)
Frame 1	3.9	10.9	27.3	0.62
Large Frame 1	3.1	9.8	28.3	0.58
Motion Average	11.3	11.6	32.5	2.31
Sum of Registered Frames	15.0	11.4	28.4	0.35
SR	13.9	12.3	25.1	0.17
SR without PSF modeling	13.3	12.4	26.2	0.81
All Counts	11.7	12.1	26.8	0.20

As expected in all of the simulated datasets used in the comparative evaluation the respiratory synchronized images led to the worst signal to noise ratio as a result of the reduced count statistics. Despite this, an improvement in the size of the detected lesions and the associated lesion contrast relative to the respiratory motion average images was measured. This improvement

	SNR T+	SNR B	Contrast T-/B
Frame 1	4.0	3.7	5.7
Large Frame 1	3.1	1.8	5.1
Motion Average	8.0	8.4	5.0
Sum of Registered Frames	8.8	9.4	6.1
SR	11.7	11.5	6.2
SR without PSF modeling	8.4	8.9	6.1
All Counts	7.6	8.4	6.2

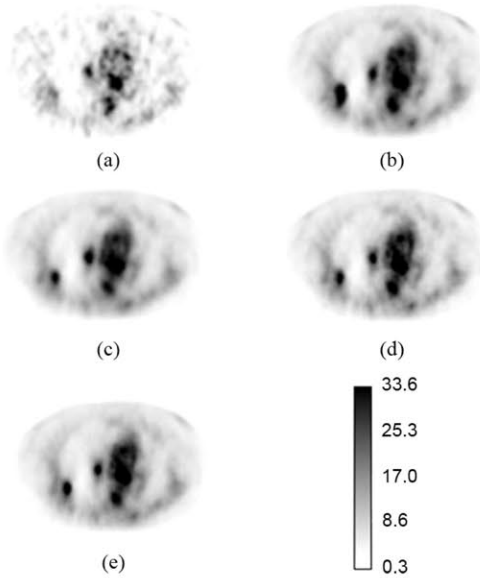|	FWHM T+ (mm)	Position error T+ (mm)	Position error T- (mm)
Frame 1	15.8	1.10	3.00
Large Frame 1	11.1	2.16	4.80
Motion Average	24.3	6.19	2.55
Sum of Registered Frames	19.0	2.37	0.75
SR	19.1	0.33	0.21
SR without PSF modeling	19.3	0.67	0.14
All Counts	18.9	0.37	0.42

Fig. 7. Single transaxial slice of the first clinical dataset showing reconstructed images corresponding to the (a) first gated frame, (b) motion average image, (c) sum of registered synchronized frames, (d) super-resolution approach, and (e) super-resolution without PSF modeling approach.
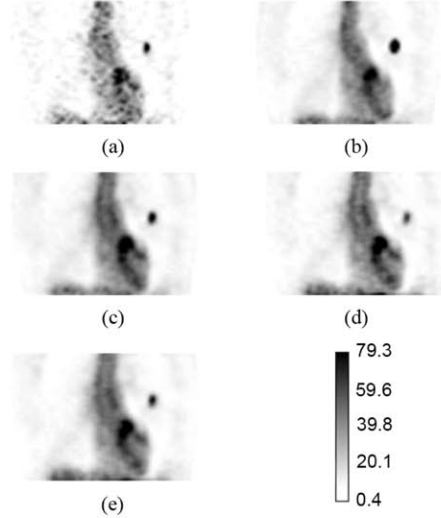

Fig. 8. Coronal views of the second clinical dataset showing reconstructed images corresponding to the (a) first gated frame, (b) motion average image, (c) sum of registered synchronized frames, (d) super-resolution approach, and (e) super-resolution without PSF modeling approach.

Patient 1 (tumor 1)	SNR B	SNR T	Contrast	FWHM (mm)
Frame 1	6.4	3.7	10.5	22.45
Motion Average	7.2	3.9	10.6	25.00
Sum of Registered Frames	7.1	4.3	12.0	23.55
SR	7.8	4.2	17.2	21.15
SR without PSF modeling	7.3	4.4	17.0	21.19
Patient 1 (tumor 2)		SNR T	Contrast	FWHM (mm)
Frame 1		17.4	51.1	33.07
Motion Average		20.7	52.1	32.04
Sum of Registered Frames		22.2	63.0	30.57
SR		22.5	70.4	30.88
SR without PSF modeling		24.7	67.8	31.08
Patient 2	SNR B	SNR T	Contrast	FWHM (mm)
Frame 1	7.2	2.9	18.3	11.77
Motion Average	7.6	3.3	21.3	12.14
Sum of Registered Frames	7.6	3.9	26.4	12.37
SR	7.9	4.2	39.0	10.30
SR without PSF modeling	7.8	3.8	37.0	10.87

was however smaller than the one achieved by the same synchronized frame image reconstructed using the same number of counts as the respiratory motion average image. These results are in agreement with previous studies by others [10].

A respiratory motion corrected image was obtained based on previously proposed approaches by summing the individually reconstructed synchronized frame images following deformable image registration [5], [6]. As expected the performance of this approach in terms of SNR as well as in determining lesion location and/or size was similar to that of the single respiratory synchronized frame using the same count statistics as the motion average image. However, one thing worth noting was the larger variability in determining the lesion size as a function of the lesion location in the lung field which was also reported by Lamare et al. [10]. This variability can be explained by a combination of two factors. The first is the limited precision of the deformable model used to align the individual synchronized frame images. Although spline-based motion models are well adapted to modeling respiratory motion [9], [10], they can fail on small structures or noisy images. The second factor is the nonuniformity of respiratory motion in the lungs. Lesions located in the lower part of the lung fields are generally associated

with a larger magnitude motion than lesions located in the upper part.

The super-resolution images calculated with and without PSF had higher SNR (by a factor of over 4 on average) and lesion contrast (by a factor of 2) than the single respiratory synchronized frame using the same reconstruction matrix size. In comparison to the motion corrected or the motion free images a similar SNR was obtained. However, the SR image without PSF modeling achieved a better performance in terms of recovered lesion contrast (up to 40%) and size (up to 10%), particularly in the case of the smaller lesions (7–11 mm). Incorporating resolution modeling in the SR model further improved contrast (3.3%±1.5%) and resolution (FWHM was 2.0%±1.8% lower). In addition, although both SR images use the same motion fields as the image obtained by summing the frames previously registered to a common position, a smaller variability in the measured lesion size with respect to the lesion location in the lung fields was seen in the standard NCAT SR images. This can be explained by the function minimized during the super-resolution process (see (9), Section II-A), where we seek to minimize the sum of differences between each synchronized frame and the super-resolution image registered to this frame. By not treating each registered frame independently, this process encourages a consistency of the registration. Our super-resolution approach should be, therefore, less dependent on the registration process accuracy than the register-and-sum technique.

The proposed approach was implemented on a standard personal computer (Intel Xeon 3 GHz dual core). The super-resolution process considering six synchronized frames of dimension $128 \times 128 \times 60$ voxels took < 100 min. For comparison the reconstruction of each individual respiratory synchronized image on the same computer took ~ 14 min.

Three previously proposed super-resolution PET enhancing methods based on the use of the IBP and POCS super-resolution algorithms involved either wobbling the detector arrays, moving the patient bed during the acquisition, or shifting the reconstruction matrix. The obvious advantage of the proposed approach is the exploitation of the respiratory motion information, which is an inherent part of the acquisition process, to improve overall image quality. In addition, this methodology does not require longer acquisition periods as is the case with the implementation requiring successive shifts of the patient bed. Furthermore, and unlike the approach consisting in shifting the reconstruction grid, the noise content in each of our frames is independent, which allows a better noise recovery in the final image.

Furthermore, previously proposed approaches for the use of super-resolution in PET concentrated on the use of the IBP and the POCS algorithms. The advantages of the MAP approach over these algorithms are threefold. First, the algorithm converges towards a unique solution. The result is thus independent of the initial image or of the number of iterations used. Second, unlike the one used in IBP, the cost function to be minimized incorporates an *a priori* term which can lead to a solution having some desirable properties chosen by the user. Finally, the blurring introduced by the finite resolution of the PET detectors can be modeled in the algorithm, which allows better resolution recovery.

There are, however, two potential pitfalls when using super-resolution to correct respiratory motion instead of using one of the previously proposed approaches. The first stems from the nonuniformity of the respiratory motion. The previous approaches led to a resolution enhancement uniform throughout the image. In our approach, however, the resolution enhancement is nonuniform and takes place only in moving parts of the image. In parts of the anatomy where there is no respiratory motion (such as for example in the spine), the sample points are the same for all gated frames. Super-resolution in these regions thus performs a mere averaging of all frames, enhancing SNR but not resolution. Thus, in this sense the resulting images have a nonuniform resolution recovery.

The second potential pitfall of the proposed approach is its dependency on the deformable registration step, which is performed independently of the super-resolution process. Inaccuracies in the registration parameters can lead to errors in the high resolution image. However, as we explained before in this section, the super-resolution step can, to some extent, compensate for inconsistencies on the registration between individual frames.

Other limitations of the current implementation of the algorithm include the performance dependency of the super-resolution image on the regularization parameters, which are currently chosen empirically, as well as the modeling of the scanner PSF as a spatially invariant Gaussian blur. Although, this simplified model was shown to yield better results in terms of contrast and resolution enhancement than the absence of blur modeling, a more accurate spatially variant PSF model might yield further resolution enhancement. Finally, consistent differences were observed in the performance of the different reconstructions in terms of the parameters considered (contrast, SNR, FWHM, and position error), demonstrating a better performance for the super-resolution reconstructed images for both simulated and clinical datasets. However, these differences were not statistically significant given the small number of both simulated and clinical datasets and the potential clinical impact of the proposed approach needs to be demonstrated in larger patient image series.

Future developments will address these issues by developing an automatic framework for the selection of optimal regularization parameters for each image sequence, and estimating the motion parameters within the super-resolution process. Within this context the alternative that will be pursued is the integration of the super-resolution process within the reconstruction of the 4-D datasets compared to its current application following the independent reconstruction of the individual respiratory synchronized frame images.

V. CONCLUSION

A MAP based super-resolution algorithm has been implemented and applied to respiratory gated images. Results on simulated datasets including realistic respiratory motion and on clinical data show that this method leads to motion compensation combined with globally improved image SNR and locally improved contrast and resolution enhancement.

REFERENCES

[1] L. Boucher, S. Rodrigue, R. Lecomte, and F. Benard, "Respiratory gating for 3-Dimensional PET of the thorax: Feasibility and initial results," *J. Nucl. Med.*, vol. 45, no. 2, pp. 214–219, Feb. 2004.

[2] D. Visvikis, D. C. Costa, I. Croasdale, A. H. R. Lonn, J. Bomanji, S. Gacinovic, and P. J. Ell, "CT-based attenuation correction in the calculation of semi-quantitative indices of [18F]FDG uptake in PET," *Eur. J. Nucl. Med. Mol. Imag.*, vol. 30, no. 3, pp. 344–53, Mar. 2003.

[3] Y. E. Erdi, S. A. Nehmeh, T. Pan, A. Pevsner, K. E. Rosenzweig, G. Mageras, E. D. Yorke, H. Schoder, W. Hsiao, O. D. Squire, P. Vernon, J. B. Ashman, H. Mostafavi, S. M. Larson, and J. L. Humm, "The CT motion quantitation of lung lesions and its impact on PET-Measured SUVs," *J. Nucl. Med.*, vol. 45, no. 8, pp. 1287–1292, Aug. 2004.

[4] S. A. Nehmeh, Y. E. Erdi, C. C. Ling, K. E. Rosenzweig, O. D. Squire, L. E. Braban, E. Ford, K. Sidhu, G. S. Mageras, S. M. Larson, and J. L. Humm, "Effect of respiratory gating on reducing lung motion artifacts in PET imaging of lung cancer," *Med. Phys.*, vol. 29, no. 3, p. 366, 2002.

[5] P. Kinahan, L. MacDonald, L. Ng, A. Alessio, P. Segars, B. Tsui, and S. Pathak, "Compensating for patient respiration in PET/CT imaging with the registered and summed phases (RASP) procedure," in *Proc. 3rd IEEE Int. Symp. Biomed. Imag.: Nano Macro*, Apr. 2006, pp. 1104–1107.

[6] M. Dawood, N. Lang, X. Jiang, and K. P. Schafers, "Lung motion correction on respiratory gated 3-D PET/CT images," *IEEE Trans. Med. Imag.*, vol. 25, no. 4, pp. 476–485, Apr. 2006.

[7] F. Lamare, T. Cresson, J. Savean, C. C. L. Rest, A. J. Reader, and D. Visvikis, "Respiratory motion correction for PET oncology applications using affine transformation of list mode data," *Phys. Med. Biol.*, vol. 52, no. 1, pp. 121–140, 2007.

[8] L. Livieratos, L. Stegger, P. M. Bloomfield, K. Schafers, D. L. Bailey, and P. G. Camici, "Rigid-body transformation of list-mode projection data for respiratory motion correction in cardiac PET," *Phys. Med. Biol.*, vol. 50, no. 14, pp. 3313–3322, Jul. 2005.

[9] F. Qiao, T. Pan, J. W. Clark, and O. R. Mawlawi, "A motion-incorporated reconstruction method for gated PET studies," *Phys. Med. Biol.*, vol. 51, pp. 3769–3783, Aug. 2006.

[10] F. Lamare, M. J. L. Carbayo, T. Cresson, G. Kontaxakis, A. Santos, C. C. L. Rest, A. J. Reader, and D. Visvikis, "List-mode-based reconstruction for respiratory motion correction in PET using non-rigid body transformations," *Phys. Med. Biol.*, vol. 52, no. 17, pp. 5187–5204, Sep. 2007.

[11] M. G. Kang and S. Chaudhuri, "Super-resolution image reconstruction," *IEEE Signal Process. Mag.*, vol. 20, no. 3, pp. 19–20, 2003.

[12] A. Dagher and C. J. Thompson, "Real-time data rebinning in PET to obtain uniformly sampled projections," *IEEE Trans. Nucl. Sci.*, vol. 32, no. 1, pp. 811–817, Feb. 1985.

[13] M. N. Wernick and C. T. Chen, "Superresolved tomography by convex projections and detector motion," *J. Opt. Soc. Am. A, Optics Image Sci.*, vol. 9, no. 9, pp. 1547–1553, Sep. 1992.

[14] J. Kennedy, O. Israel, A. Frenkel, R. Bar-Shalom, and H. Azhari, "Super-resolution in PET imaging," *IEEE Trans. Med. Imag.*, vol. 25, no. 2, pp. 137–147, Feb. 2006.

[15] J. A. Kennedy, O. Israel, A. Frenkel, R. Bar-Shalom, and H. Azhari, "Improved image fusion in PET/CT using hybrid image reconstruction and super-resolution," *Int. J. Biomed. Imag.*, 2007.

[16] G. Chang, T. Pan, J. W. Clark, and O. R. Mawlawi, "Optimization of super-resolution processing using incomplete image sets in PET imaging," *Med. Phys.*, vol. 35, no. 12, p. 5748, 2008.

[17] G. Chang, T. Pan, F. Qiao, J. W. Clark, and O. R. Mawlawi, "Comparison between two super-resolution implementations in PET imaging," *Med. Phys.*, vol. 36, no. 4, p. 1370, 2009.

[18] M. Irani and S. Peleg, "Improving resolution by image registration," *Graphical Models Image Process. (CVGIP)*, vol. 53, no. 3, pp. 231–239, 1991.

[19] H. Stark and P. Oskoui, "High-resolution image recovery from image-plane arrays, using convex projections," *Opt. Soc. Am., J. A: Opt. Image Sci.*, vol. 6, pp. 1715–1726, Nov. 1989.

[20] J. L. Rubio-Guivernau, M. J. Ledesma-Carbayo, F. Lamare, J. E. Ortuno, P. Guerra, D. Visvikis, A. Santos, and G. Kontaxakis, "Respiratory motion correction in PET with super-resolution techniques and non-rigid registration," in *IEEE Nucl. Sci. Symp. Conf. Rec.*, 2007, vol. 5, pp. 3560–3563.

[21] R. Schultz and R. L. Stevenson, "A Bayesian approach to image expansion for improved definition," *IEEE Trans. Image Process.*, vol. 3, no. 3, pp. 233–242, May 1994.

[22] R. Schultz and R. L. Stevenson, "Bayesian image and video enhancement using a non-Gaussian prior," in *Nonlinear Signal ands Image Processing: Theory, Methods and Applications*, K. Barner and G. Arce, Eds. Boca Raton, FL: CRC, 2004, pp. 295–332.

[23] D. P. Capel and A. Zisserman, "Super-resolution enhancement of text image sequence," in *Int. Conf. Pattern Recognit.*, 2000, pp. 600–605.

[24] J. Kybic and M. Unser, "Fast parametric elastic image registration," *IEEE Trans. Image Process.*, vol. 12, no. 11, pp. 1427–1442, Nov. 2003.

[25] F. Lamare, A. Turzo, Y. Bizais, C. C. L. Rest, and D. Visvikis, "Validation of a Monte Carlo simulation of the Philips Allegro/GEMINI PET systems using gate," *Phys. Med. Biol.*, vol. 51, no. 4, pp. 943–962, Feb. 2006.

[26] K. Jordan, IEC emission phantom appendix performance evaluation of positron emission tomographs Med. Public Health Res. Program Eur. Commun., 1990.

[27] W. Segars, D. Lalush, and B. Tsui, "Modeling respiratory mechanics in the MCAT and spline-based MCAT phantoms," *IEEE Trans. Nucl. Sci.*, vol. 48, no. 1, pp. 89–97, Feb. 2001.

[28] A. Reader, S. Ally, F. Bakatselos, R. Manavaki, R. Walledge, A. Jeavons, P. Julyan, S. Zhao, D. Hastings, and J. Zweit, "One-pass list-mode EM algorithm for high-resolution 3-D PET image reconstruction into large arrays," *IEEE Trans. Nucl. Sci.*, vol. 49, no. 3, pp. 693–699, Jun. 2002.

[29] A. L. Maitre, W. Segars, S. Marache, A. Reilhac, M. Hatt, S. Tomei, C. Lartizien, and D. Visvikis, "Incorporating patient-specific variability in the simulation of realistic whole-body [18F]FDG distributions for oncology applications," *Proc. IEEE*, vol. 97, no. 12, pp. 2026–2038, Dec. 2009.